CHEMISTRY OF MATERIALS

Article

pubs.acs.org/cm

Electrical and Optical Properties of Sb-Doped $BaSnO_3$

Hiroshi Mizoguchi,[†,⊥] Ping Chen,[‡,⊗] Punit Boolchand,[‡] Vadim Ksenofontov,[§] Claudia Felser,[§] Paris W. Barnes,[∥] and Patrick M. Woodward*[,†]

[†]Department of Chemistry, The Ohio State University, Columbus, Ohio 43210-1185, United States

[‡]Department of Electrical and Computer Engineering and Computer Science, University of Cincinnati, Cincinnati, Ohio 45221-0030, United States

[§]Institut fuer Anorganische Chemie und Analytische Chemie, Johannes Gutenberg-Universitaet Mainz, D 55099 Mainz, Germany

[∥]Department of Chemistry, Millikin University, Decatur, Illinois 62522, United States

ABSTRACT: The electronic and optical properties of the cubic perovskite, $BaSnO_3$, are compared with the well-known transparent conducting oxides (TCOs), SnO_2 and In_2O_3. The optical band gaps of the undoped compounds, as measured by diffuse reflectance spectroscopy on powdered samples, are 3.1 eV for $BaSnO_3$ and 3.8 eV for SnO_2. Electronic structure calculations show that both compounds possess a large conduction band dispersion, which suggests that $BaSnO_3$, like SnO_2, should be a good TCO if it can be n-doped. To explore this possibility the properties of substitutionally doped, $BaSn_{1-x}Sb_xO_3$ samples were investigated. The electrical conductivity increases drastically for $BaSn_{1-x}Sb_xO_3$ samples with $x \leq 0.05$, showing a transition from an insulating to a metallic state. For higher doping levels, $0.05 < x < 0.15$, the conductivity saturates at 4 S cm^{-1}. This is accompanied by saturation in the expansion of the cubic lattice parameter. The color of the pellets changed from white ($x = 0$) to bluish black ($x = 0.15$). This darkening originates from the formation of an intense and broad optical absorption band centered at 1200−1300 nm for the more highly doped samples. This absorption band spans both the visible and the near-infrared regions, resulting in a loss of transparency. Various spectroscopic techniques were used to elucidate the observed behavior. Mössbauer spectroscopy reveals the presence of mixed valent antimony, $Sb^{3+}(5s^2)/Sb^{5+}(5s^0)$, as x increases. ESR spectra collected on a $BaSn_{0.99}Sb_{0.01}O_3$ sample indicate that only ∼5% of unpaired electrons are present as delocalized carriers. The other 95% are localized to form a Sn^{3+} trapped electron center. To explain the tendency for carrier localization in doped $BaSnO_3$ a mechanism based on strong electron−phonon interactions in perovskites containing cations with $(n - 1)d^{10}ns^0$ electronic configuration is proposed. This mechanism explains why $BaSn_{1-x}Sb_xO_3$ possesses relatively poor TCO characteristics, in sharp contrast to widely used TCO materials $Sn_{1-x}Sb_xO_2$ and $In_{1-x}Sn_xO_{1.5}$.

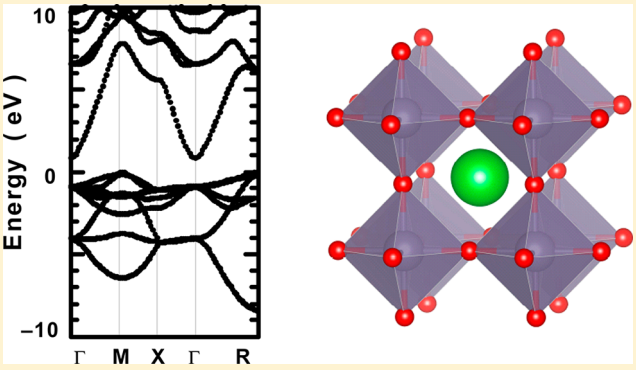

KEYWORDS: *transparent conductive oxides, perovskite oxides, mixed valence compounds, Mössbauer spectroscopy*

INTRODUCTION

There are relatively few materials that are simultaneously transparent to visible light (or a portion of the visible spectrum) and good conductors of electricity. Most of the materials that do display this behavior are n-doped metal oxides, such as In_2O_3 ($InO_{1.5}$), ZnO, and SnO_2. These materials are collectively referred to as transparent conducting oxides (TCO) materials. TCOs are utilized in a wide variety of products from photovoltaics to antistatic coatings, but the two dominant applications are flat-panel displays and energy-efficient windows.[1] Fluorine-doped SnO_2 is the most widely utilized material for energy-efficient window coatings, while tin-doped $InO_{1.5}$ (ITO) dominates the market for flat panel displays.

Despite the widespread applications of TCOs, the structural and compositional features that are favorable for transparent conductivity are not fully understood. It is widely accepted that the best n-type TCO materials contain a metal with a $(n - 1)d^{10}ns^0np^0$ electronic configuration. Despite the greatly expanded compositional space, ternary oxides have not been investigated for their TCO properties in nearly the same detail as binary oxide TCOs. One of the first studies of ternary oxides as TCOs was carried out by Shannon, Gilson, and Bouchard in 1977.[2] In subsequent years TCO behavior has been found among oxides from the spinel family, such as $MgIn_2O_4$.[3] Exploration of multicomponent phase diagrams, such as $InO_{1.5}-SnO_2-ZnO-CdO-Ga_2O_3$, have yielded a number of new TCO candidate materials.[4] With the exception of ZnO, the structures of most TCOs contain infinite networks of edge-sharing octahedra.

Received: June 14, 2013
Revised: August 15, 2013
Published: August 29, 2013

   dx.doi.org/10.1021/cm4019309 | *Chem. Mater.* 2013, 25, 3858−3866

Perovskites are one of the most important families of ternary oxides. Perovskites exhibit a wide range of electrical properties including superconductivity, colossal magnetoresistance, ferroelectricity, piezoelectricity, ionic conductivity, and so forth. However, there have been relatively few investigations of perovskites as transparent conductors. One exception is the orthorhombic perovskite $CdSnO_3$ which was shown to be a transparent conductor almost 20 years ago.[2] However, further explorations of this material as a TCO have not ensued. Perhaps in part because of concerns with the toxicity of cadmium and the polymorphism of this compound. More recently the band gaps and electronic structures of a number of perovskites containing $(n-1)d^{10}ns^0np^0$ cations have been investigated.[5] These studies suggest that the conduction band dispersion and band gap of $BaSnO_3$ should be similar to $CdSnO_3$ and motivated this study of the electrical and optical properties of Sb-doped $BaSnO_3$ as a potential ternary TCO material. In fact, La-doped $SrGeO_3$ with perovskite-type structure has been recently reported as an n-type TCO,[6] despite the fact that Ge oxides are typically insulators.

Perovskites tend to readily form solid solutions, which is favorable for attempts to introduce carriers through substitutional doping. Previous work has shown that it is possible to n-dope $BaSnO_3$ through Sb substitution onto the Sn site, as well as La substitution onto the Ba site.[7] In particular it has been shown that antimony has a large solubility, 18%. Furthermore, in the corresponding binary TCO system, $Sn_{1-x}Sb_xO_2$ is known to form wide range solid solution through wet chemical, low temperature synthetic routes.[8] This provides an opportunity to directly compare the properties of doped $BaSnO_3$ and SnO_2.

Figure 1 shows the band structure diagrams for $BaSnO_3$ and SnO_2 on the same scale.[5,9] For n-type TCOs the lowest energy conduction band (CB) is the most important band. The dispersion of this band determines the mobility of the charge carriers, which is critical for TCO applications. In both $BaSnO_3$ and SnO_2 this band originates primarily from Sn 5s−O 2p σ^* orbital interactions. However, translational symmetry prevents mixing of the Sn 5s and O 2p orbitals at the Γ-point. As a result this band becomes predominantly Sn 5s nonbonding at Γ. The change from antibonding to nonbonding character is responsible for the large dispersion of this band. A more detailed analysis of band structures of these oxides can be found in refs 5 and 9. The similarities of the $BaSnO_3$ and SnO_2 CBs suggest that $BaSnO_3$ should exhibit high carrier mobility if it can be n-doped.

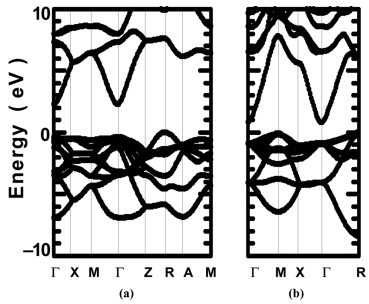

Figure 1. Calculated band structures of (a) SnO_2 and (b) $BaSnO_3$. The binding energy (E = 0) is referenced to the valence band maximum. For SnO_2, Γ = (0, 0, 0), X = (1/2, 0, 0), M = (1/2, 1/2, 0), Z = (0, 0, 1/2), R = (1/2, 0, 1/2), and A = (1/2, 1/2, 1/2). For $BaSnO_3$, Γ = (0, 0, 0), M = (1/2, 1/2, 0), X = (1/2, 0, 0), and R = (1/2, 1/2, 1/2).

EXPERIMENTAL SECTION

SnO_2 (99.9%, Fisher), $BaCO_3$ (99.4%, Mallinckrodt), Sb_2O_3 (99.9%, Cerac), and In_2O_3 (99.9%, Cerac) were used as reagents. $BaSn_{1-x}Sb_xO_3$ ($0 \le x \le 0.15$) and $In_{1-x}Sn_xO_{1.5}$ ($0.03 \le x \le 0.06$) were synthesized via solid-state reaction at elevated temperature. These materials were mixed with ethanol and ground in an agate mortar and pestle. The mixture for $BaSn_{1-x}Sb_xO_3$ was first calcined at 1473 K for 10 h in air to decompose the carbonates. After this initial firing, the products were ground and pressed into pellets uniaxially (30 kpsi). This was followed by cold isostatic pressing (60 kpsi, American Isostatic Presses Inc., Columbus, OH) and heating at 1723 or 1823 K for 15 h in air. For all heat treatments Pt crucibles were employed and the pellets were buried in loose powder to reduce the potential loss of antimony. Cation stoichiometries were confirmed by inductively coupled plasma analysis. For $In_{1-x}Sn_xO_{1.5}$, the mixture of reagents was heated at 1773 K for 10 h in air.

The phase purity was confirmed with laboratory X-ray powder diffraction (XRPD). A Bruker D8 diffactometer (40 kV, 50 mA) was used to collect the XRPD data. It is equipped with a Braun linear position sensitive detector and an incident beam Ge 111 monochromator which provides high resolution data in addition to eliminating the Cu K_β and $K_{\alpha 2}$ radiation. The Rietveld method,[10] as implemented in the TOPAS software package,[11] was used for the structural analysis of the XRPD data. High resolution time-of-flight neutron powder diffraction (NPD) data were collected at the Special Environmental Powder Diffractometer (SEPD) at Argonne National Laboratory.[12] Rietveld refinements were completed on data collected using detector bank #1 (2θ = 144°) using the EXPGUI/GSAS software package.[13]

Standard four probe electrical conductivity measurements were made over the temperature range 300−40 K within a closed cycle cryostat. Ohmic contacts to the polycrystalline pellets were formed by applying an In−Ga alloy to the surface. UV−vis−NIR diffuse reflectance data were collected over the spectral range 240−2600 nm with a Perkin-Elmer Lamda 900 double-beam spectrometer with MgO as the reference material. The data were transformed into absorbance with the Kubelka−Munk function. Electrochemical measurements were done in a standard three electrode cell, with a Pt counterelectrode and a Ag/AgCl reference electrode in 0.1 M Na_2SO_4 aqueous solution. The $BaSn_{1-x}Sb_xO_3$ (x = 0.01) pellet, which acted as the working electrode, was irradiated by a 150 W xenon lamp through a quartz window and a mechanical shutter. For characterization of defect centers, electron spin resonance (ESR) spectra were collected at 300 and 110 K with a Bruker ESP300 X-band spectrometer. The g values of signals were calibrated to the signal of DPPH (g = 2.0036) as an internal standard. Spin concentration were determined from the second integral of the spectrum using $CuSO_4 \cdot 5H_2O$ as a standard. ^{119}Sn Mössbauer spectra of the powdered samples were collected at 77 K using ^{119m}Sn in $CaSnO_3$ as an emitter. ^{121}Sb Mössbauer spectra of the powdered samples were collected at 4.2 K using ^{121m}Sn in $CaSnO_3$ as an emitter.

RESULTS

Appearance and Conductivity. Table 1 shows the composition, color, and density for the samples obtained. The undoped $BaSnO_3$ sample is white, but the color changes drastically from blue to bluish black, as x increases. The increase of x improved sintering properties, as previously reported by Cava et al.[14] ICP analysis suggests moderate volatilization of Sn resulting in slightly higher Sb content than synthetically targeted. However, we have elected to identify samples by their nominal antimony concentration throughout this manuscript.

dx.doi.org/10.1021/cm4019309 | Chem. Mater. 2013, 25, 3858−3866

Table 1. Cationic Compositions, Color, and Density of the Samples, $BaSn_{1-x}Sb_xO_3$

	ICP analysis (rel. mole frac.)			
x	Sn (%)	Sb (%)	color	density/theoretical X-ray density(%)
0	100	0	white	49
0.05	92	8	blue	59
0.10	86	14	bluish black	69
0.15	80	20	bluish black	83

The evolution of the electrical conductivity with changes in doping and temperature are shown in Figures 2 and 3. Pure

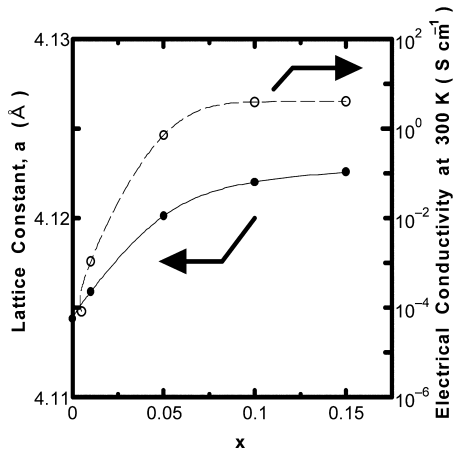

Figure 2. Lattice constants for $BaSn_{1-x}Sb_xO_3$ estimated from Rietveld refinements for X-ray powder diffraction patterns. Error bars are smaller than the symbols. The x dependence of electrical conductivity at 300 K is also shown.

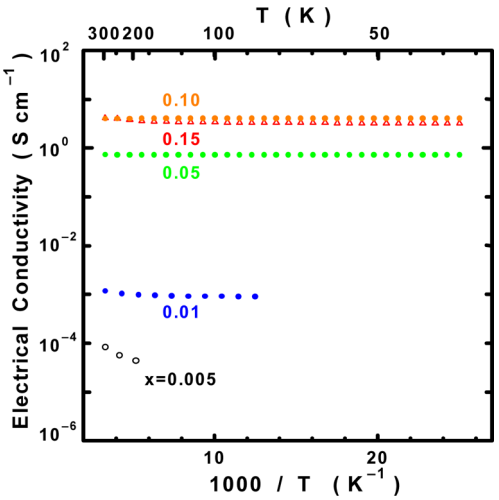

Figure 3. Temperature dependence of electrical conductivity of $BaSn_{1-x}Sb_xO_3$.

$BaSnO_3$ ($x = 0$) is a white insulator whose resistance is too high to be measured with our instrumental setup. A drastic increase in conductivity at 300 K is observed as x increases. The conductivity increases with increasing temperature for the x = 0.005 sample, and to a lesser extent for the x = 0.01 sample, indicating activated carrier transport. For the more heavily doped samples (x = 0.05, 0.10, and 0.15) the conductivity is temperature independent, indicating a degenerately doped semiconductor. The increase in conductivity begins to level off around x = 0.05 and saturates at 4 S cm^{-1} around x = 0.10. Pellets with different relative densities showed similar conductivities, which suggests that the values plotted in Figure 3 are not heavily influenced by grain boundaries. This is particularly true for the x = 0.10 and x = 0.15 samples. The changes in conductivity with increased doping are in qualitative agreement with Cava et al. who reported a bell shape profile for conductivity vs x, with maximum value 10 S cm^{-1} at x = 0.10.[14]

The room temperature conductivity of $In_{1-x}Sn_xO_{1.5}$ thin films has been reported to be 5×10^3 S cm^{-1} for x = 0.05. This value is in reasonable agreement with a conductivity of 9×10^2 S cm^{-1} (T = 298 K) measured for an $In_{1-x}Sn_xO_{1.5}$ (x = 0.06) pellet prepared as part of this study. These values are two orders higher than our polycrystalline $BaSn_{1-x}Sb_xO_3$ pellets. Seebeck coefficients on $BaSn_{1-x}Sb_xO_3$ pellets were measured to be −80, −24, −26, and −26 μV K^{-1} at 300 K for x = 0.01, 0.05, 0.10, and 0.15 samples, respectively. The negative Seebeck coefficients confirm that these compounds are n-type semiconductors, as are $Sn_{1-x}Sb_xO_2$ and $In_{1-x}Sn_xO_{1.5}$.

Structure and Composition. The x = 0 sample showed sharp diffraction peaks corresponding to the simple cubic perovskite structure ($Pm\bar{3}m$). X-ray powder diffraction analysis showed that Sb-doped samples are also cubic as there was no sign of peak splitting or extra reflections that are indicative of the symmetry-lowering that commonly occurs in perovskites as a result of octahedral tilting.[15] Lattice parameters were extracted from the XRPD data using the Rietveld method, and the results are shown in Figure 2. The unit cell initially expands in response to Sb-doping, but the slope starts to decrease around x = 0.05, and there is little change for $x \geq 0.10$. The same general trend was reported by Cava et al.[14] and Huang et al.[16] Note how the saturation of the unit cell expansion correlates rather well with the saturation of conductivity seen with increasing x. For $BaSn_{1-x}Sb_xO_3$ samples with x = 0.18 and 0.20 diffraction peaks due to an unknown second phase appeared, suggesting that the solid solubility limit occurs near x = 0.15. In an attempt to increase the Sb solubility, the sample with x = 0.18 was heated at 1823 K and quenched into water. However, even with this procedure we were not able to suppress the formation of the second phase.

In oxides, attempts to introduce charge carriers through substitutional doping of an aliovalent cation are often frustrated by the presence of charge compensating defects. This behavior is well-known in perovskites[17] where examples of both anion vacancies, AMO_{3-x}, and cation vacancies, $(AM)_{1-x}O_3$ or AMO_{3+x}, are known. In oxides, antimony typically adopts either the 3+ ($4d^{10}5s^25p^0$) or the 5+ ($4d^{10}5s^05p^0$) oxidation state. This raises the possibility that Sb-substitution does not introduce carriers as intended. If Sb^{3+} substitutes on the Sn^{4+} site charge compensation can be realized via the formation of oxygen vacancies, $BaSn_{1-x}Sb^{3+}{}_xO_{3-x/2}$. Conversely, Sb^{5+} substitution could be compensated by cation vacancies, $Ba(Sn_{1-x}Sb^{5+}{}_x)_{1-y}O_3$. As an independent assessment of the stoichiometry NPD data were collected and analyzed. The neutron cross sections for Ba, Sn, Sb, and O are 5.1, 6.2, 5.6, and 5.8 fm, respectively. While not useful to assess the Sb/Sn ratio neutron diffraction should be sensitive to the presence of either cation or anion vacancies. The results for the refinements of occupancy factors for Ba, Sn, and Sb are shown in Table 2. The Rietveld analysis did not show evidence for an appreciable concentrations of either type of vacancy.

dx.doi.org/10.1021/cm4019309 | Chem. Mater. 2013, 25, 3858−3866

Table 2. . Crystal Structure of $BaSn_{1-x}Sb_xO_y$ (x = 0–0.15) As Determined by NPD[a]

nominal x in $BaSn_{1-x}Sb_xO_3$	U (Ba)	U (Sn/Sb)	U_{11} (O)	$U_{22} = U_{33}$ (O)	O occ.	R_p (%)	R_{wp} (%)	χ^2
0	0.0051(1)	0.0035(1)	0.0031(2)	0.0103(2)	0.996(3)	4.97	7.54	1.935
0.01	0.0052(1)	0.0035(1)	0.0036(2)	0.0101(2)	0.992(3)	5.00	7.51	2.066
0.05	0.0055(2)	0.0035(1)	0.0037(3)	0.0101(2)	0.991(3)	4.72	7.17	1.856
0.10	0.0059(2)	0.0036(1)	0.0045(2)	0.0104(2)	0.996(3)	4.57	6.96	1.891
0.15	0.0068(2)	0.0036(1)	0.0052(3)	0.0109(2)	1.004(3)	4.73	7.08	1.756

[a]Occupancy factors for oxygen were refined. The Rietveld refinements were carried out using space group $Pm\bar{3}m$.

Photoelectrochemical Response. Figure 4 shows the polarization curve for $BaSn_{1-x}Sb_xO_3$ (x = 0.01) in 0.1 M Na_2SO_4(aq). There is a clear photocurrent, but unfortunately the response as a function of applied voltage is not very sharp. One of the origins might be low density of the sintered pellet that acts as the electrode (55% relative to theoretical X-ray density). Nevertheless, the data are of sufficient quality to make an estimate of −0.25 V vs Ag/AgCl for the flat band potential. The estimated band positions in aqueous solution referenced to the standard hydrogen electrode (SHE) at pH = 0 are shown in the inset of Figure 4, together with those of SnO_2 as a comparison. The positions of the band edges were estimated by assuming the flatband potential is located at the bottom of the CB. The bandgap values obtained from diffuse reflectance measurements can then be used to locate the top of valence band. Based on these measurements, the flatband potential of $BaSnO_3$ is estimated to be 0.1 eV deeper than that of SnO_2.

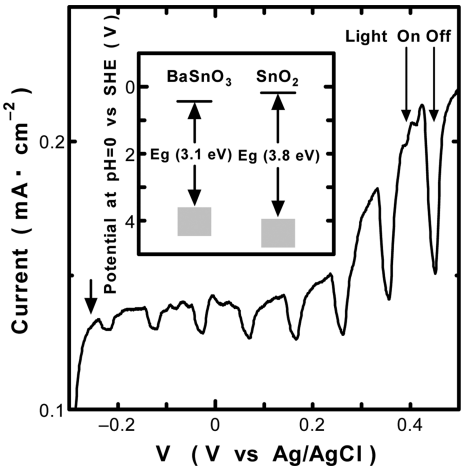

Figure 4. Photoelectrochemical properties of a $BaSn_{1-x}Sb_xO_3$ (x = 0.01) polycrystalline electrode. It was irradiated with a non-monochromatic Xe lamp (150 W). The electrolyte was 0.1 M Na_2SO_4. The inset shows the position of the CB minimum and valence band maximum of $BaSnO_3$, compared with SnO_2.

Optical Absorption. The diffuse reflectance spectra for $In_{1-x}Sn_xO_{1.5}$ (x = 0.0, 0.03, 0.06) are shown in Figure 5a. Pure indium oxide, $InO_{1.5}$ has symmetry forbidden direct fundamental gap, as revealed by first principles calculations.[18] Our measurements reveal an absorption edge around 400 nm (3.1 eV). When tin is introduced the absorption spectra change dramatically. The carriers introduced by Sn-doping give rise to plasmon excitations that obey the Drude model and lead to absorbance in the infrared region of the spectrum. The x = 0.03 sample ($\sigma_{298\ K}$ = 2 × 10^2 S cm^{-1}) shows a maximum absorbance near 2000 nm, while the absorbance of the x = 0.06 sample ($\sigma_{298\ K}$ = 9 × 10^2 S cm^{-1}) reaches a maximum near 1700 nm. The shift of this peak to higher energy is expected

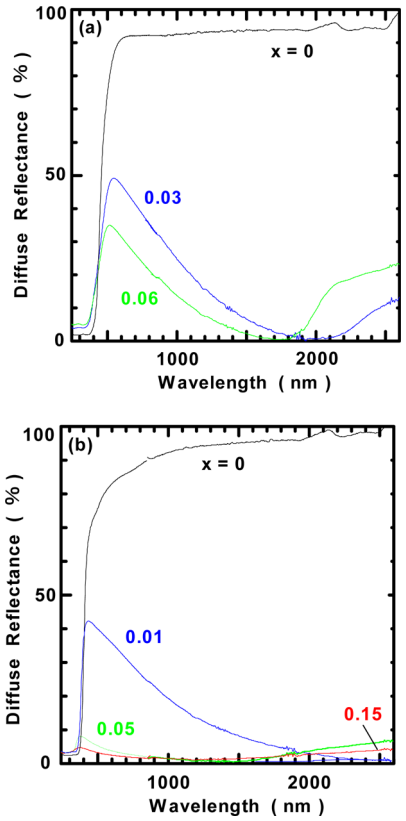

Figure 5. Diffuse reflectance spectra for (a) $In_{1-x}Sn_xO_{1.5}$ and (b) $BaSn_{1-x}Sb_xO_3$.

from the higher carrier concentration of the x = 0.06 sample. The absorptions due to plasmon excitations tail into the visible region impacting the color. If a sample absorbs light at both ends of visible light region, a green color is expected. The color will shift to blue, violet, and finally black as the transparent window region shifts to higher energy, because of shifts of both the absorption edge and the plasmon tail. In this study, the color of the powdered samples changes from yellow to green to bluish green, as x increases.

The increase of diffuse reflectance in the region 1900–2600 nm was observed for the x = 0.06 sample. The large influence on the diffuse reflectance spectrum by spectral reflection seen in the NIR prevents us from applying the Kubelka–Munk function, which makes it difficult to determine the plasma frequency (ω_p) accurately from the diffuse reflectance spectra.[19] However, Cox et al. determined ω_p for polycrystalline $In_{1-x}Sn_xO_{1.5}$ pellets directly, using electron energy loss spectroscopy (EELS).[20] They reported ω_p = 0.50 eV (2480 nm) for x = 0.01, 0.60 eV (2070 nm) for x = 0.04, and 0.65 eV (1910 nm) for x = 0.06. These values are qualitatively consistent with our diffuse reflectance spectra.

dx.doi.org/10.1021/cm4019309 | Chem. Mater. 2013, 25, 3858–3866

The diffuse reflectance spectra for $BaSn_{1-x}Sb_xO_3$ are shown in Figure 5b. The $x = 0$ sample shows a clear absorption edge at 400 nm, indicating bandgap of 3.1 eV. As x increases the diffuse reflectance in the NIR region sharply decreases. As a result the tail of the plasmon absorption moves into the visible region, resulting in the blue color of the powders. Even the substitution of 1% Sb ($x = 0.01$) decreased the peak intensity for diffuse reflectance to 42%. The rate for darkening in $BaSn_{1-x}Sb_xO_3$ is much higher than observed for $In_{1-x}Sn_xO_{1.5}$ (the peak intensity for the $x = 0.03$ sample was 50%.). In other words, for equivalent amounts of dopant the transparency in $BaSn_{1-x}Sb_xO_3$ is inferior to $In_{1-x}Sn_xO_{1.5}$. Careful observation shows that the bandgap absorption edge shifts to higher energy (i.e., blue shift) as x increases. This is the so-called Burstein–Moss shift which is a characteristic feature of good TCOs. It indicates a large CB dispersion.

As x increases further, intense darkening was observed for $BaSn_{1-x}Sb_xO_3$. The peak intensity for diffuse reflectance decreased to 8% in the $x = 0.05$ sample, which means that most of the transparency to visible light has been lost. By the time x reaches 0.10, the samples become black and transparency in the visible region is negligible. The spectra for $x = 0.05–0.15$ show an upturn in the reflectance (less absorbance) in the 2000–2600 nm range. While this spectral feature is similar to that seen in $In_{1-x}Sn_xO_{1.5}$, the absorption mechanisms are likely to be different. First of all, the rise in reflectance for wavelengths greater than 2000 nm (originating from the influence of spectral reflection) observed in $In_{1-x}Sn_xO_{1.5}$ is much steeper than that of $BaSn_{1-x}Sb_xO_3$. Also, the conductivity for $BaSn_{1-x}Sb_xO_3$ which is related to ω_p is two orders lower than that of $In_{1-x}Sn_xO_{1.5}$. For these reasons we suspect that the NIR absorbance seen in the more heavily doped $BaSn_{1-x}Sb_xO_3$ samples does not arise solely from excitations of the free carriers.

ESR. Electron spin resonance (ESR) measurements on $BaSn_{1-x}Sb_xO_3$ powders were carried out at 300 and 110 K to probe for the formation of unpaired electrons resulting from Sb-substitution. Figure 6a shows the ESR spectra for $x = 0$ and $x = 0.01$ at 110 K, respectively. The $BaSnO_3$ sample ($x = 0$) prepared at 1723 K showed a complicated ESR spectrum at 110 K. Signals were found at g values of 1.76 (a very weak peak at ~3700 G) and near 2.002 (a much stronger peak at ~3350 G). As x increased, the intensities for both peaks increased, as shown in Figure 6a. The $g = 2.002$ peak has fine structures, as shown in Figure 6b, and increased the line width as x increases, resulting in the loss of fine structure. The $g = 1.76$ peak showed gradual increase of the g-value as x increases (inset of Figure 6a), as well as an increase of peak intensity.

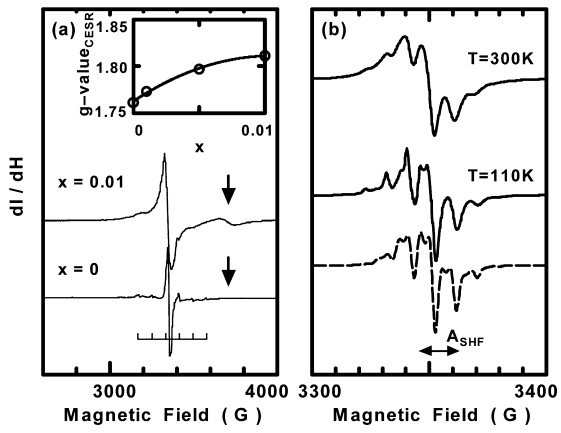

Figure 6. (a) ESR spectra (solid lines) measured at 110 K on the $BaSn_{1-x}Sb_xO_3$ powder sample with $x = 0$ and 0.01 made by solid state reaction at 1723 K. The inset shows the dependence on x of the g value of the conduction electron around 3750 G. (b) ESR spectra (solid lines) measured at 300 and 110 K on the $BaSnO_3$ powder sample ($x = 0$). The experimental spectra are compared with the simulated powder pattern (dotted line) using the parameters $g_{\|} = 2.0044$, $g_{\perp} = 2.0008$, A (HF, Sn) = 0 G, and A (SHF, Sn) = 18.0 G.

As a side note the sample with $x = 0$ made at 1723 K did show a very weak sextet signal that we attribute to Mn^{4+} (Figure 6a). The presence of manganese is thought to originate from one of the furnaces used for synthesis, judging from the fact that the sample made at 1473 K in a different furnace did not contain the Mn^{4+} ESR signal. To investigate the possibility that manganese contamination might be linked to the six peaks, $BaSn_{1-x}Mn_xO_3$ ($x = 0.001$, 0.005, 0.01, and 0.02) samples were intentionally prepared. ESR spectra of these samples confirm that the sextet signal originates from Mn^{4+}.[21]

It is well-known that the g-value of conduction electrons in TCOs typically deviates from g_e (free electron). Examples include $g = 1.77–1.80$ for CdO, 1.88 for $InO_{1.5}$, 1.87–1.90 for SnO_2, 1.90 for $CdSnO_3$ (perovskite type), and 1.86–1.89 for Cd_2SnO_4.[22] The g-value combined with the lack of structure allows us to confidently assign the weak $g = 1.76$ peak in the $BaSnO_3$ sample to free carriers in the CB, and the amount of spin is 2×10^{19} cm^{-3}. On the other hand, the $g = 2.002$ signal with strong intensity shows no shift in g-value, as x increases. This peak is thought to correspond to a localized center. The signal at 300 and 110 K is magnified in Figure 6b. The complicated shape of the signal implies that the wave function of the unpaired electron even at 110 K extends over multiple but finite number of tin sites.[23] Because the g-value is close to g_e, we cannot easily justify whether this is due to an electron or a positive hole from the Pryce equation. However, the g-value agreed with that observed for n-doped $BaSn_{1-x}Sb_xO_3$ samples ($x = 0.005$ and 0.01) shown in Figure 6a, and the intensity increased as x increased. Thus, we considered this to be an electron center.

To simulate the ESR spectrum for $x = 0$ at 110 K, we have made the assumption that this is a Sn^{3+} ($= Sn^{4+} + e^-$) center in the perovskite lattice surrounded by six nearest neighbor Sn^{4+} ions, mediated by O^{2-} ions ($I = 0$). Thus, the spectrum is influenced from both a strong hyperfine (HF) interaction of the central Sn ion ($I = 1/2$), as well as a superhyperfine (SHF) interaction by the six nearest neighbor Sn ions ($I = 1/2$), located at the distance of 4.11 Å. The SHF coupling constant is taken to be isotropic because of the long Sn–Sn distance (4.11 Å). The simulation for powder pattern for the central Sn ($I = 0$) was carried out for the spectrum of $x = 0$, using the same method as employed by Watanabe et al.[24] The simulated spectrum obtained in this way using axial g values is shown in Figure 6b by dotted line, which shows reasonable agreement with the experimental pattern. We did not consider the influence by the central Sn ion ($I = 1/2$, HF) in this simulation because we could not detect any splitting in the peak(s) arising from the central Sn ion ($I = 1/2$), despite the fact that the 50–10000 G magnetic field region was investigated. There are two reasons why the detection of this splitting is difficult to observe. One is the relatively high measurement temperature. The other is the small natural abundance, 16.54%, of Sn ions with $I = 1/2$.[25] The obtained SHF coupling constant, 18 G from the six nearest neighbor Sn ions ($I = 1/2$) with the distance 4.11 Å,

dx.doi.org/10.1021/cm4019309 | Chem. Mater. 2013, 25, 3858–3866

seems to be reasonable, taking into consideration a value of 34 G observed as an SHF coupling constant in Mn-doped SnO_2 with Mn−Sn distance, 3.12 Å.[26] On the basis of this simulation, we ascribe the signal around 3350 G to the Sn^{3+} electron trapped center in the octahedral site of the perovskite structure. The trapped electron might be strongly coupled with the formation of an oxygen vacancy for $x = 0$. As $x > 0$, the signal became broad and lost structure because of the increase of spin concentration. The total amount of spin detected in each measurement is in qualitative agreement with the nominal Sb-content of the samples. From the ratio of the peak areas we estimate that 95% of the unpaired electrons are trapped on the Sn^{3+} site for the $x = 0.01$ sample. This result gives some insight into why $BaSn_{1-x}Sb_xO_3$ samples are not more conducting.

Mössbauer Spectroscopy. ^{119}Sn Mössbauer spectroscopy is an excellent probe of the local environment and oxidation state of tin. This method gives us two primary pieces of information, isomer shift (IS) and quadruple splitting (QS). The isomer shift gives us the information about the valence state of the Sn ion. The quadrupole splitting (QS) gives us information about the symmetry around the probe ion (Sn). We selected $BaSnO_3$ as a reference of the isomer shift. Figure 7

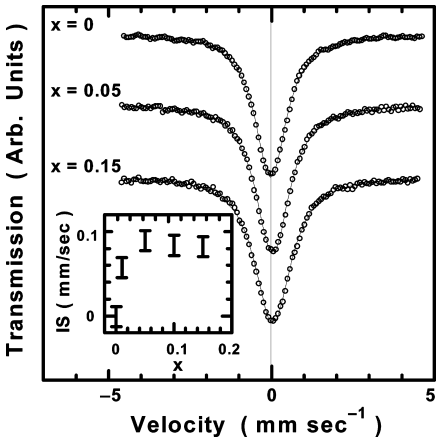

Figure 7. ^{119}Sn Mössbauer spectra of $BaSn_{1-x}Sb_xO_3$ at 77 K. The reference is $BaSnO_3$. The inset shows the x dependence for the isomer shift.

shows the ^{119}Sn Mössbauer spectra for $BaSn_{1-x}Sb_xO_3$. Each spectrum for x shows a simple peak, and it was possible to fit this using a single Lorentzian curve with QS = 0. (Fitting curve is shown with a solid line.) This indicates that a SnO_6 coordination with O_h symmetry and a homogeneous single state for Sn ion are retained after Sb-substitution. This is consistent with the $Pm\bar{3}m$ space group symmetry estimated from XRPD and NPD. The Sn ion takes usually Sn^{4+} ($4d^{10}5s^05p^0$) or Sn^{2+} ($4d^{10}5s^25p^0$) in oxides. It is known that Sn^{4+} and Sn^{2+} show isomer shifts of −0.4 to +2.0 mm sec^{-1} and 2.3 to 4.5 mm sec^{-1} (relative to $BaSnO_3$), respectively.[27] The IS values observed for $BaSn_{1-x}Sb_xO_3$ ($0 < x < 0.15$) fell in the range expected for Sn^{4+}, although there was a slight increase in IS in the doped samples, as shown in the inset of Figure 7. Peaks associated with Sn^{2+} were not observed. This subtle shift in the IS translates to an increase of the s electron density. In other words, the Sn ion is reduced slightly as x increases, as suggested by the ESR. However, the reduction appears to saturate by the time x reaches 0.05. This result is similar to the change of lattice constant and the electrical conductivity (Figure 2). These results are similar to ^{119}Sn Mössbauer data for $Sn_{1-x}Sb_xO_2$ reported by other groups, where the homogeneous reduction of the Sn^{4+} ion without the formation of Sn^{2+} has also been reported.[28−30]

The Sb ion takes usually Sb^{3+} ($4d^{10}5s^25p^0$) or Sb^{5+} ($4d^{10}5s^05p^0$) in oxides. There are many characterization methods for the Sb ion, for example, XPS, XANES. Among these, ^{121}Sb Mössbauer is useful for the separation of Sb^{3+}/Sb^{5+} owing to the large difference in the IS of Sb^{3+} and Sb^{5+}. For ^{121}Sb Mössbauer, the transition from the ground state nuclear with $I = 5/2$ to excited state nuclear with $I = 7/2$ is detected. Both ground and excited states have axial symmetry, and thus have an electric quadruple. Therefore, when the symmetry around the Sb ion for the electric field gradient decreases from cubic (O_h), the levels for ground states split into three, ± 5/2, ± 3/2, ± 1/2. Similarly, excited states split into four, ± 7/2, ± 5/2, ± 3/2, ± 1/2. These bring about the splitting of absorption spectra into eight (or twelve), because of the transition rule ($\Delta m_I = 0, \pm 1$) and give us the information about the symmetry around probe ion (Sb).

The IS for Sb is large, and was observed for −11.0 mm·sec^{-1} or 0.6 mm·sec^{-1} relative to Sb for Sb_2O_3 or Sb_2O_5 respectively.[30,31] Figure 8 shows the ^{121}Sb Mössbauer spectra

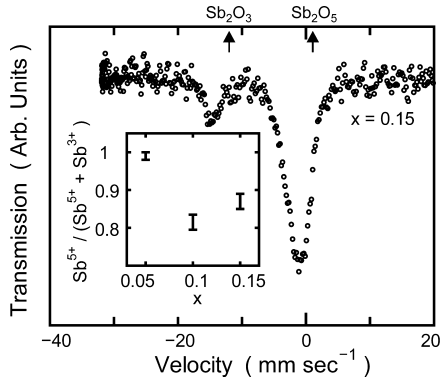

Figure 8. ^{121}Sb Mössbauer spectra of $BaSn_{1-x}Sb_xO_3$ at 4.2 K. The reference is Sb metal. The inset shows the x dependence for the fraction of Sb^{5+}.

at 4.2 K for $BaSn_{1-x}Sb_xO_3$ powder. The strong peak around −1.2 mm sec^{-1} for $x = 0.15$ is ascribed to the Sb^{5+} state. The eight (or twelve) peaks are not resolved, and a single broad peak results. The weak peak around −14.0 mm sec^{-1} is assigned to Sb^{3+}. The ratio of the area for the two peaks agrees with the ratio of the concentrations. It is noted that the IS for both peaks is quite different from that for Sb^{4+} which is observed in $BaPb_{1-x}Sb_xO_3$.[32] While the content of Sb^{3+} is only 1(1)% for $x = 0.05$, it increased to ∼15% for $x > 0.10$, forming a mixed valence (MV) state of the $5s^0-5s^2$ type, resulting in an inactive dopant state. These behaviors for the Sb ion as well as Sn ion are very similar to those for $Sn_{1-x}Sb_xO_2$ reported by other groups.[28,30,33]

The Mössbauer results clearly show that when carriers localize, Sb^{3+} is formed in preference to Sn^{2+}. This is as expected given the higher effective nuclear charges of the Sb^{5+} ion with respect to the Sn^{4+} ion.

DISCUSSION

Before the discussion on the microscopic mechanism associated with Sb-substitution, let us summarize briefly the physical

dx.doi.org/10.1021/cm4019309 | Chem. Mater. 2013, 25, 3858−3866

properties observed for $BaSn_{1-x}Sb_xO_3$. In the region $0 < x < 0.05$, the conductivity increases drastically as x increases, and temperature dependent conductivity is observed. Strong absorbance in the NIR region was observed, indicating the existence of free carriers. A Burstein−Moss shift is observed for diffuse reflectance spectra confirming the large dispersion of CB for $BaSnO_3$ predicted by band structure calculations. However, the conductivity never becomes as large as seen in good TCO materials, and the transparency in the visible region quickly disappears as x increases. For samples with $0.05 < x < 0.15$ the conductivity saturates at roughly 4 S cm^{-1}. The shape of the spectral response in the NIR changes for $x = 0.05$ and 0.10 samples. A new, very broad absorption band appears around 1200−1300 nm. This absorption causes the sample to lose transparency in the vis−NIR region.

What is the origin of the low conductivity? Let us select $x = 0.01$ as an example. The conductivity was measured as 1×10^{-3} S cm^{-1}. The low conductivity must originate either from low carrier concentration or low mobility: $\sigma = en\mu$ (σ, electrical conductivity; n, carrier concentration; and μ, carrier mobility). As a first approximation we can take the free carrier concentration n to be 2×10^{19} cm^{-3}, which was estimated by ESR. The equation gives $\mu = 3 \times 10^{-4}$ cm^2 V^{-1} s^{-1}. This value is extremely small relative to that for known TCOs, such as SnO_2 thin film (20 cm^2 V^{-1} s^{-1}), Sn and Mg doped $InO_{1.5}$ thin film (30 cm^2 V^{-1} s^{-1}), $In_{1-x}Sn_xO_{1.5}$ pellet (80 cm^2 V^{-1} s^{-1}), CdO thin film (120 cm^2 V^{-1} s^{-1}), and β-PbO_2 (90 cm^2 V^{-1} s^{-1}).[34] Thus, we can conclude that μ for $BaSn_{1-x}Sb_xO_3$ ($x = 0.01$) is much smaller than for $In_{1-x}Sn_xO_{1.5}$.[35]

One possible origin for the small conductivity of the $BaSn_{1-x}Sb_xO_3$ samples is Sb^{3+}/Sb^{5+} mixed valency in the $0.10 < x < 0.15$ region. ^{121}Sb Mössbauer spectra suggested that only ∼70% Sb is active as a dopant (Figure 8 inset). Nonetheless, the observed low conductivity in the $x < 0.05$ region cannot be attributed entirely to the Sb MV state. For $x = 0.01$, ^{119}Sn Mössbauer gives no evidence for Sn^{2+} and extrapolation of the ^{121}Sb Mössbauer results suggest a rather low concentration of Sb^{3+}. However, ESR measurements show that 95% of the unpaired electrons are localized, nominally on a Sn^{3+} site. Even taking into account that 19 out of every 20 carriers are localized, the conductivity is much lower than that of TCOs like $InO_{1.5}$ and SnO_2 doped at a comparable level.

What is the origin for low μ? Changes in the band structure as a result of Sb-substitution, including the subtle increase in lattice parameter and impurity scattering events, undoubtedly lead to a small decrease in carrier mobility. However, such mechanisms are also at play in other doped TCO materials whose mobilities are 4−5 orders of magnitude higher. Hence these mechanisms are not likely to be the reason for the low carrier mobility. Instead we propose the electron−phonon interaction as the origin for the low μ. Strong electron phonon interaction is well-known for cations with ns^2 electronic configuration.[36] Day and co-workers showed strong intervalence charge transfer (IVCT) transitions in the metal complex such as Cs_2SbCl_6 (= $Cs_4Sb^{3+}Sb^{5+}Cl_{12}$), where there is an electronic transition from Sb^{3+} to Sb^{5+} mediated by intervening lattice vibrations of the anion. They classified compounds which show a characteristic electronic transition between MV cations as class II MV compounds. Many halides fall into this category. In oxides cationic ns^2 electrons tend to localize to form a cationic lone pair, as observed in α-PbO (litharge). Occasionally Bi^{3+} has relatively regular octahedral coordination in oxides, but similar environments have little precedent for Sb^{3+} in oxides. The distorted perovskite $BaBiO_3$ (= $Ba_2Bi^{3+}Bi^{5+}O_6$), the mother phase for high T_c superconductors $BaBi_{1-x}Pb_xO_3$ and $Ba_{1-x}K_xBiO_3$, is one of the few examples.[37] Large $Bi^{3+}O_6$ octahedra alternate with smaller $Bi^{5+}O_6$ octahedra in $BaBiO_3$. The strong electron−phonon coupling that leads to the Bi^{3+}/Bi^{5+} charge ordering makes $Ba_2Bi^{3+}Bi^{5+}O_6$ an insulator. In $BaBiO_3$ the so-called breathing mode that creates different environments for Bi^{3+} and Bi^{5+} ions is static (frozen). When such lattice vibrations become dynamic they can couple with electron transfer from an ns^2 ion to an ns^0 ion in which case the carrier transport is said to be polaronic.[38] This typically results in a large electron effective mass and low carrier mobility. The lattice vibration mode greatly enhances IVCT absorption. Therefore, it seems plausible to ascribe the broad absorption band centered on 1200−1300 nm that is seen for $BaSn_{1-x}Sb_xO_3$ with $x = 0.05$−0.15 to an IVCT band. The Sn^{3+} electron center for $x = 0.01$ detected by ESR might be associated with this mechanism. However, it is noted that there are few reports for Sn^{2+}/Sn^{4+} MV oxides except for $Sn_2M_2O_{7+x}$ (M = Nb,Ta).[39] The Sb^{3+}/Sb^{5+} MV is much more stable in solid oxides. But, $Sb^{3+}O_6$ octahedra in perovskite-type oxides are usually highly distorted, because the cationic $5s^2$ lone pair has a tendency to localize. And, this also enhances the decrease of the carrier mobility.

Finally, we compare the observed effects by Sb substitution in $BaSnO_3$ with those for other TCOs. Sn substitution into $InO_{1.5}$ is possible up to $x \sim 10\%$ for the polycrystalline solid. Phenomena similar to those seen in $BaSn_{1-x}Sb_xO_3$ are observed for the evolution of the lattice parameter and electrical conductivity as x increases. In $In_{1-x}Sn_xO_{1.5}$ thin films, the slope of lattice constant starts to decrease around $x = 0.03$ and saturates around $x = 0.08$−0.10, where the second phase $In_4Sn_3O_{12}$ begins to appear. $In_{1-x}Sn_xO_{1.5}$ (thin film/pellet) and $BaSn_{1-x}Sb_xO_3$ also show saturation near $x = 0.10$. In $In_{1-x}Sn_xO_{1.5}$ powder ^{119}Sn Mössbauer spectra show that the Sn^{4+} state is kept up to $x = 0.10$.[40] The saturation is thought to originate from incorporation of excess oxygen ions, which reduce the carrier concentration.[41] This suggests that the observed phenomena are similar with $BaSn_{1-x}Sb_xO_3$, although the mechanisms are different.

CONCLUSION

The solid solubility of Sb in $BaSn_{1-x}Sb_xO_3$ extends up to ∼15% substitution. The cubic perovskite structure is maintained over the entire range. In the region $0 < x < 0.05$, the conductivity increases drastically as x increases, and temperature independent conductivity is observed. Unfortunately the conductivity never reaches values seen in good TCO materials, and the transparency in the visible region quickly disappears as x increases. For higher doping levels the conductivity saturates, and a very broad absorption band appears around 1200−1300 nm associated with IVCT excitations.

The behavior of $BaSn_{1-x}Sb_xO_3$ has important implications for the design of TCOs. Although oxides containing corner-sharing octahedra can possess wide CBs that in principle should result in high carrier mobility and good TCO characteristics, they suffer from a fatal flaw. In structures, like the cubic perovskite structure of $BaSnO_3$, containing linear metal−oxygen−metal bonds the CB width is at a maximum. Unfortunately, this type of framework is favorable for IVCT transitions between p-block cations. This leads to strong electron−phonon coupling that reduces the carrier mobility, and a strong IVCT optical absorption that reduces the

dx.doi.org/10.1021/cm4019309 | Chem. Mater. 2013, 25, 3858−3866

transparency. The problems of the IVCT are lessened in $CdSnO_3$, which has a highly distorted perovskite structure with Sn−O−Sn angles (~140 deg) that are far from linear. However, in such ternary oxides a large CB dispersion can only be realized if both cations are p-block ions.

AUTHOR INFORMATION

Corresponding Author

*E-mail: woodward@chemistry.ohio-state.edu.

Present Addresses

[⊥]Tokyo Institute of Technology, Frontier Research Center, Yokohama 226-8503, Japan.

[⊗]Boise State University, Boise, Idaho.

Notes

The authors declare no competing financial interest.

ACKNOWLEDGMENTS

First we must thank Dr. G. D. Renkes, Dr. R. L. McCreery, and Dr. A. M. Nowak (The Ohio State University), T. Maeda, and Dr. K. Ueda (Kyushu Institute of Technology) for experimental support. Dr. H. Kawazoe (Tokyo Institute of Technology) provided valuable guidance for ESR analysis. We are also grateful to the late Dr. J. D. Jorgensen (Argonne National Laboratory) for the support of NPD.

REFERENCES

(1) (a) Ginley, D. S.; Bright, C. *MRS Bull.* **2000**, *25*, 15. (b) *Handbook of Transparent Conductors*; Ginley, D. S., Hosono, H., Paine, D., Eds.; Springer: New York, 2010.

(2) Shannon, R. D.; Gillson, J. L.; Bouchard, R. J. *J. Phys. Chem. Solids* **1977**, *38*, 877.

(3) (a) Kawazoe, H.; Ueda, N.; Un'no, H.; Omata, T.; Hosono, H.; Tanoue, H. *J. Appl. Phys.* **1994**, *76*, 7935. (b) Kawazoe, H.; Ueda, K. *J. Am. Ceram. Soc.* **1999**, *82*, 3330.

(4) (a) Minami, T.; Kakuma, T.; Takeda, Y.; Takata, S. *Thin Solid Films* **1998**, *317*, 326. (b) Metz, A. W.; Ireland, J. R.; Zheng, J.; Lobo, R. P. S. M.; Yang, Y.; Ni, J.; Stern, C. L.; Dravid, V. P.; Bontemps, N.; Kannewurf, C. R.; Poeppelmeier, K. R.; Marks, T. J. *J. Am. Chem. Soc.* **2004**, *126*, 8477. (c) Hosono, H. *Thin Solid Films* **2007**, *515*, 6000. (d) Harvey, S. P.; Poeppelmeier, K. R.; Mason, T. O. *J. Am. Ceram. Soc.* **2008**, *91*, 3683. (e) Hoel, C. A.; Mason, T. O.; Gaillard, J. F.; Poeppelmeier, K. R. *Chem. Mater.* **2010**, *22*, 3569.

(5) (a) Woodward, P. M.; Mizoguchi, H.; Kim, Y.-I.; Stoltzfus, M. W. In *Metal Oxides*; Fierro, J. L. G., Ed.; Taylor & Francis: Boca Raton, FL, 2006; p 133. (b) Mizoguchi, H.; Eng, H. W.; Woodward, P. M. *Inorg. Chem.* **2004**, *43*, 1667.

(6) Mizoguchi, H.; Kamiya, T.; Matsuishi, S.; Hosono, H. *Nat. Commun.* **2011**, *2*, 470.

(7) (a) Trari, M.; Doumerc, J.-P.; Dordor, P.; Pouchard, M.; Behr, G.; Krabbes, G. *J. Phys. Chem. Solids* **1994**, *55*, 1239. (b) Larramona, G.; Gutierrez, C.; Pereira, I.; Nunes, M. R.; da Costa, M. A. *J. Chem. Soc., Faraday Trans. I* **1989**, *85*, 907. (c) Pereira, I.; Melo, M. J.; da Costa, M. A.; Nunes, M. R.; Peter, L. M. *J. Chem. Soc., Faraday Trans. I* **1989**, *85*, 2473. (d) Herrmann, J.-M.; Nunes, M. R.; da Costa, F. M. A. *J. Chem. Soc., Faraday Trans. I* **1982**, *78*, 1983. (e) Smith, M. G.; Goodenough, J. B.; Manthiram, A.; Taylor, R. D.; Peng, W.; Kimball, C. W. *J. Solid State Chem.* **1992**, *98*, 181. (f) Wang, H. F.; Liu, Q. Z.; Chen, F.; Gao, G. Y.; Wu, W.; Chen, X. H. *J. Appl. Phys.* **2007**, *101*, 106105.

(8) Pyke, D.; Reid, R.; Tilley, R. J. D. *J. Chem. Soc., Faraday Trans. I* **1980**, *76*, 1174.

(9) Mizoguchi, H.; Woodward, P. M. *Chem. Mater.* **2004**, *16*, 5233.

(10) Young, R. A., Ed.; *The Rietveld Method*; Oxford University Press: Oxford, U.K., 1995.

(11) Cheary, R. W.; Coelho, A. A. *J. Appl. Crystallogr.* **1992**, *25*, 109.

(12) Jorgensen, J. D.; Faber, J., Jr; Carpenter, J. M.; Crawford, R. K.; Haumann, J. R.; Hitterman, R. L.; Kleb, R.; Ostroski, G. E.; Rotella, F. J.; Worlton, T. G. *J. Appl. Crystallogr.* **1989**, *22*, 321.

(13) (a) Toby, B. H. *J. Appl. Crystallogr.* **2001**, *34*, 210. (b) Larson, A. C.; Von Dreele, R. B. *General Structure Analysis System (GSAS)*, LANL Report LAUR 86-748; Los Alamos National Laboratory: Los Alamos, NM, 1994.

(14) Cava, R. J.; Gammel, P.; Batlogg, B.; Krajewski, J. J.; Peck, W. F., Jr; Feldel, R.; Van Dover, R. B. *Phys. Rev. B* **1990**, *42*, 4815.

(15) (a) Woodward, P. M. *Acta Crystallogr., Sect. B* **1997**, *53*, 44. (b) Lufaso, M. W.; Woodward, P. M. *Acta Crystallogr., Sect. B* **2001**, *57*, 725.

(16) Huang, T.; Nakamura, T.; Itoh, M.; Inaguma, Y.; Ishiyama, O. *J. Mater. Sci.* **1995**, *30*, 1556.

(17) (a) Barret, A. A.; Jacobson, A. J.; Tofield, B. C.; Fender, B. E. *Acta Crystallogr., Sect. B* **1982**, *38*, 2775. (b) Van Roosmalen, J. A. M.; Cordfunke, E. H. P.; Helmholdt, R. B.; Zandbergen, H. W. *J. Solid State Chem.* **1994**, *110*, 100.

(18) (a) Weiher, R. L.; Ley, R. P. *J. Appl. Phys.* **1966**, *37*, 299. (b) Enhart, P.; Klein, A.; Egdell, R. G.; Albe, K. *Phys. Rev. B* **2007**, *75*, 153205. (c) Walsh, A.; Da Silva, J. L. F.; Wei, S.-H.; Korber, C.; Klein, A.; Piper, L. F. J.; DeMasi, A.; Smith, K. E.; Panaccione, G.; Torelli, P.; Payne, D. J.; Bourlange, A.; Egdell, R. G. *Phys. Rev. Lett.* **2008**, *100*, 167402.

(19) (a) Mizoguchi, H.; Fukumi, K.; Kitamura, N.; Takeuchi, T.; Hayakawa, J.; Yamanaka, H.; Yanagi, H.; Hosono, H.; Kawazoe, H. *J. Appl. Phys.* **1999**, *85*, 6502. (b) Mizoguchi, H.; Kitamura, N.; Fukumi, K.; Mihara, T.; Nishii, J.; Nakamura, M.; Kikuchi, N.; Hosono, H.; Kawazoe, H. *J. Appl. Phys.* **2000**, *87*, 4617.

(20) Cox, P. A.; Fravell, W. R.; Egdell, R. G. *J. Solid State Chem.* **1987**, *68*, 340.

(21) Balamurugan, K.; Kumar, N. H.; Ramachandran, B.; Rao, M. S. R.; Chelvane, J. A.; Santhosh, P. N. *Solid State Commun.* **2009**, *149*, 884.

(22) (a) Muller, K. A.; Schneider, J. *Phys. Lett.* **1963**, *4*, 288. (b) Walsh, W. M.; Remeika, J. P.; Rupp, L. W., Jr. *Phys. Rev.* **1966**, *152*, 223. (c) Elschner, B.; Schlaak, M. *Phys. Lett.* **1967**, *24A*, 10. (d) Nagasawa, M.; Shionoya, S. *J. Phys. Soc. Jpn.* **1971**, *30*, 158. (e) Golestani-Fard, F.; Mackenzie, K. J. D. *J. Mater. Sci. Lett.* **1984**, *3*, 403. (f) Meinhold, R. H. *J. Phys. Chem. Solids* **1987**, *48*, 927. (g) Gulino, A.; Fragala, I. *J. Mater. Chem.* **1999**, *9*, 2837.

(23) There are several nuclei for Sn which have nuclear spin: ^{115}Sn I = 1/2 (N. A. = 0.35%), ^{117}Sn I = 1/2 (N. A. = 7.61%), ^{119}Sn I = 1/2 (N. A. = 8.58%).

(24) Watanabe, Y.; Kanazawa, T.; Kawazoe, H. *J. Non-Cryst. Solids* **1985**, *71*, 279.

(25) An electron-trapped center, Cd^+ in CdO detected by ESR has been reported by Elschner and Schlaak.[22c] This is a trapped electron on a Cd^{2+} ion. In this report, the detection of HF splitting because of the central Cd ion (I = 1/2) was not observed at 100 K, despite the relatively high natural abundance, 25.01%, of cadmium nuclei with I = 1/2. Therefore, the lack of splitting originating from HF coupling of the central Sn ion (I = 1/2) in $BaSnO_3$ at 110 K does not seem to be unreasonable.

(26) From, W. H.; Dorain, P. B.; Kikuchi, C. *Phys. Rev.* **1964**, *135A*, 740.

(27) Greenwood, N. N.; Gibb, T. C. *Mössbauer Spectroscopy*; Chapman and Hall: London, U.K., 1971.

(28) Birchall, T.; Bouchard, R. J.; Shannon, R. D. *Can. J. Chem.* **1973**, *51*, 2077.

(29) Berry, F. J.; Maddock, A. G. *Inorg. Chim. Acta* **1978**, *31*, 181.

(30) Portefaix, J. L.; Bussiere, P.; Forissier, M.; Figueras, F.; Freiedt, J. M.; Sanchez, J. P.; Theobald, F. *J. Chem. Soc., Faraday Trans. I* **1980**, *76*, 1652.

(31) Wooten, J. B.; Long, G. G.; Bowen, L. H. *J. Inorg. Nucl. Chem.* **1974**, *36*, 2177.

(32) (a) Eibschutz, M.; Reiff, W. M.; Cava, R. J.; Krajewski, J. J.; Peck, W. F., Jr *Appl. Phys. Lett.* **1990**, *56*, 2339. (b) Bente, K.; Blum, W. J.; Gaebel, R.; Pebler, J.; Schmid-Beurmann, P. *Phys. C* **1992**, *202*, 379.

(33) (a) Berry, F. J.; Holbourn, P. E.; Woodhams, F. W. D. *J. Chem. Soc., Dalton Trans.* **1980**, 2241. (b) Berry, F. J.; Laundy, B. J. *J. Chem. Soc., Dalton Trans.* **1981**, 1442.
(34) (a) Mindt, W. *J. Electrochem. Soc.* **1969**, *116*, 1076. (b) Bruneaux, J.; Cachet, H.; Froment, M.; Messad, A. *Electrochim. Acta* **1994**, *39*, 1251. (c) Omata, T.; Fijiwara, H.; Otsuka-Yao-Matsuo, S.; Ono, N.; Ikawa, H. *Jpn. J. Appl. Phys.* **1998**, *37*, L879. (d) Ni, J.; Wang, L.; Yang, Y.; Yan, H.; Jin, S.; Marks, T. J.; Ireland, J. R.; Kannewurf, C. R. *Inorg. Chem.* **2005**, *44*, 6071. (e) Yang, Y.; Jin, S.; Medvedeva, J. E.; Ireland, J. R.; Metz, A. W.; Ni, J.; Hersam, M. C.; Freeman, A. J.; Marks, T. J. *J. Am. Chem. Soc.* **2005**, *127*, 8796.
(35) The same calculation was done for homemade $In_{1-x}Sn_xO_{1.5}$ pellet (x = 0.03, $\sigma = 2 \times 10^2$ S cm^{-1}) which the density is low, ≈60% of theoretical X-ray density. μ =1 cm^2 V^{-1} s^{-1} is obtained from the n_{theory} (9.3×10^{20} cm^{-3})
(36) Day, P. *Int. Rev. Phys. Chem.* **1981**, *1*, 149.
(37) Cox, D. E.; Sleight, A. W. *Acta Crystallogr., Sect. B* **1979**, *35*, 1.
(38) (a) Sugai, S.; Uchida, S.; Kitazawa, K.; Tanaka, S.; Katsui, A. *Phys. Rev. Lett.* **1985**, *55*, 426. (b) Sugai, S. *Phys. Rev. B* **1987**, *35*, 3621.
(39) (a) Birchall, T.; Sleight, A. W. *J. Solid State Chem.* **1975**, *13*, 118. (b) Mizoguchi, H.; Wattiaux, A.; Kykyneshi, R.; Tate, J.; Sleight, A. W.; Subramanian, M. A. *Mater. Res. Bull.* **2008**, *43*, 1943.
(40) Yamada, N.; Yasui, I.; Shigesato, Y.; Li, H.; Ujihara, Y.; Nomura, K. *Jpn. J. Appl. Phys.* **1999**, *38*, 2856.
(41) Frank, G.; Kostlin, H. *Appl. Phys. A: Mater. Sci. Process.* **1982**, *27*, 197.